



Transient three-dimensional simulation of densification process of carbon fibre preforms via chemical vapour infiltration of carbon matrix from methane



Zhepeng Tang^{a,b}, Aijun Li^b, Tomo Hatakeyama^a, Hiroki Shuto^a, Jun-ichiro Hayashi^a, Koyo Norinaga^{a,c,*}

^a Institute for Materials Chemistry and Engineering of Kyushu University, 816-8580 Fukuoka, Japan

^b Research Center for Composite Materials of Shanghai University, 200072 Shanghai, China

^c Department of Chemical Systems Engineering, Graduate School of Engineering, Nagoya University, 464-8603 Nagoya, Japan

HIGHLIGHTS

- 2D woven cloth and random distributed felt were infiltrated.
- A novel pore structure evolution model was proposed.
- Simulation couples multi-step reaction model with pore structure evolution model.
- Transient 3D simulation of CVI process was successfully implemented.
- Predicted results of bulk density agree well with experimental results.

ARTICLE INFO

Article history:

Received 3 July 2017

Received in revised form 22 September 2017

Accepted 21 October 2017

Available online 23 October 2017

Keywords:

C/C composites

Chemical vapour infiltration

Transient 3D simulation

Porous structure

Numerical modelling

ABSTRACT

Chemical vapour infiltration (CVI) is widely used for fabricating carbon fibre-reinforced carbon materials for aircraft brake disks. This study aims at developing a numerical simulation method for predicting densification of the material during the CVI. Based on the multi-step reaction and deposition models, including the hydrogen inhibition model of pyrocarbon growth, transient 3D simulations of the CVI using methane as a precursor of the pyrocarbon were carried out via the finite element method coupling the mass transfer (by convection and diffusion) and the evolutive porous structure model with gas-phase and surface chemical reactions. The CVI of two different types of preforms was studied. The pore structure evolution models were derived not analytically but numerically with the aid of a computational tool for visualizing the fibre structures. An acceptable agreement was found between the predicted densification profiles and the experimental data obtained using a laboratory CVI reactor at a temperature of 1343 K, a methane pressure of 30 kPa and a total deposition time of 120 h.

© 2017 Elsevier Ltd. All rights reserved.

1. Introduction

Chemical vapour infiltration (CVI) for fabricating fibre-reinforced carbon matrix composites is a method that is used to infiltrate pyrolytic carbon (pyrocarbon) matrix into the porous fibre preform via hydrocarbon pyrolysis (Chand, 2000; Delhaes, 2002; Golecki, 1997; Vignoles, 2015a,b; Yan and Xu, 2010). The isothermal and isobaric CVI (ICVI) process is one of the common commercial methods for producing the carbon/carbon (C/C) composite, which is an extremely complicated process (Zhang and

Hüttinger, 2001). Generally, the gas phase reactions of the reactant gas molecules, surface reactions of precursors at active sites on the fibre surface, diffusion or convection of the gaseous species in the reactor, and pore structure evolution of the carbon preform occur simultaneously during the infiltration process (Vignoles et al., 2001, 2007). The primary objective for fabricating the C/C composite via the CVI process is to reduce the infiltration time while maintaining its high and uniform density (Vignoles, 2015a,b). Unfortunately, there is an inherent competition between the diffusion of the gaseous species and the pyrocarbon deposition during the progressive densification of the porous preform (Besmann et al., 1991, 1996; Roman and Stinton, 1995). Time-dependent structural characteristics of the carbon preform, e.g., equivalent radius of pore, tortuosity, total porosity, and surface area to volume

* Corresponding author at: Department of Chemical Systems Engineering, Graduate School of Engineering, Nagoya University, 464-8603 Nagoya, Japan.

E-mail address: norinaga@nagoya-u.jp (K. Norinaga).

Nomenclature

Symbols used

ρ [kg m ⁻³]	density
μ [Pa s]	dynamic viscosity
u [m s ⁻¹]	velocity
u_0 [m s ⁻¹]	inlet velocity
p [Pa]	pressure
c_i [mol m ⁻³]	concentration of species i
c_0 [mol m ⁻³]	initial concentration of methane
D_i [m ² s ⁻¹]	Fick diffusion coefficient of species i
R_i [mol m ⁻³ s ⁻¹]	chemical reaction term of species i in the free flow channel
$R_{i(sv)}$ [mol m ⁻³ s ⁻¹]	chemical reaction term of species i in preform
D_i^{eff} [m ² s ⁻¹]	effective diffusion coefficient of species i
M_C [g mol ⁻¹]	molar mass of carbon

ξ [-]	porosity
ξ_0 [-]	initial porosity
ρ_0 [g cm ⁻³]	initial density of the preform
ρ_C 1.95 [g cm ⁻³]	pyrocarbon density
$R_{C(sv)}$ [mol m ⁻³ s ⁻¹]	chemical reaction term of pyrolytic carbon in preform
k_i [s ⁻¹] or [m s ⁻¹]	reaction rate constant for reaction i
T [K]	temperature
V_i [cm ³ mol ⁻¹]	volume increment for species i
M_i [g mol ⁻¹]	molar mass of species i
δ [Å]	collision diameter
T^* [-]	reduced temperature
$\Omega(T^*)$ [-]	collision integral
ϵ/κ [K]	maximum energy of attraction divided by Boltzmann constant

ratio constantly change, which dramatically prevents the gaseous species from diffusing into the inner part of the preform. Accordingly, the early surface pore closure is inevitably formed during the industrial production process, and the intermediate machining steps are recommended to open the closed surface pores of the preform (Ibrahim and Paolucci, 2011). The numerical simulation of the CVI process based on detailed models for the chemical reactions and mass transport are expected to shed light on the underlying laws of the infiltration process, which further support the development and optimization of the production process of C/C composites (Li et al., 2008; Norinaga and Deutschmann, 2007; Tang et al., 2014).

Complex pore networks normally exist in the carbon preform, as observed using X-ray computed tomography (Kastner et al., 2012; Kinney et al., 1993; Panerai et al., 2015), which is also applied to assess the geometrical and transport properties of the preform at various stages of infiltration (Coindreau et al., 2011). As an alternative method to the computed tomography, many idealized pore models have been developed to analyse pore filling during the CVI process, such as the cylindrical pore model (Birakayala and Evans, 2002), random overlap model (Currier, 1991; Guan et al., 2013) and the node-percolation model (Starr, 1995). However, these models fail to give a sufficiently appropriate description to the evolution of various pore structural parameters among different fibre architectures during the progress of CVI. In contrast to the drawbacks, the pore structure evolution model, as in this study, is the real-time simulation with a three-dimensional visualization of the pore topology evolution during the densification process based on the approximation of the growing solid phase (Pfrang et al., 2007). The structural characteristics of the preform in three dimensions (3D) during the CVI process are then accurately computed via this model. This numerical method allows researchers to build complex architectures of the carbon preform and obtain the related structural characteristics and gas transport properties.

The properties of C/C composites are controlled by the fibre preform, the deposited matrix and the interaction between the preform and matrix (Wu et al., 2017). The preform itself, as the backbone of the C/C composite, plays the key role for the strength and stiffness of the composite (Fitzer, 1987). Consequently, for the first time, the two-dimensional (2D) woven cloth and randomly distributed felt are used as research subjects to analyse and compare the pore structure evolution and densification process between these two types of preforms. The present study aims at developing a general and efficient method for simulating the CVI process for various carbon fibre preforms. The pore structure evolution

and related structural characteristics of these two preforms were first numerically visualized by the approximation of the growing solid phase in the CVI process. Second, based on the above-proposed pore structure evolution model with the multi-step chemical reaction model from our previous study (Li et al., 2008), the CVI simulation of the preforms was realized by coupling the convection-diffusion equations, the Navier-Stokes equation of the laminar flow. Finally, as for the ICVI process to fabricate C/C composite using methane, the experimental results from a laboratory CVI reactor were compared with the predictions for evaluating the developed numerical simulation critically.

2. Experimental setup

Fig. 1 sketches the laboratory scale CVI reactor for the fabrication of C/C composite. Rectangular-shaped pitch-based 2D woven cloth or carbon fibre felt with a dimension of 36 mm (length) \times 16 mm (width) \times 58 mm (height) was fitted in a sample holder made of graphite. The narrow zone between the graphite tube and the sample holder was treated as the gas flow channel. The carbon fibre preforms were densified from methane (99.99%), which was supplied from the bottom of the reactor. The initial bulk density, fibre diameter and porosity of the cloth preform were 0.65 g/cm³, 7 μ m and 63%, respectively; for the felt preform, they were 0.12 g/cm³, 13 μ m and 93%, respectively. The CVI experiments were performed at 1343 K, 30 kPa, for 0–120 h of densification. The residence time of methane through the narrow channel was 0.4 s (cloth) or 0.5 s (felt). The experiments were conducted by changing the infiltration time, and then the time-dependent change in weight gain due to the CVI was measured. The simplified 3D geometry of the CVI reactor for the simulation of the infiltration process is shown on the top right-hand side of Fig. 1. To save the computation time, the geometry of the 3D CVI reactor was simplified into one-quarter of the original with consideration of symmetry.

3. Methodology

3.1. Reaction model

Due to the time-consumption and convergence problem using the detailed reaction mechanism, a simplified chemical reaction model (Becker and Hüttinger, 1998) was applied to simulate both the methane pyrolysis and carbon deposition in the reactor, as shown in Fig. 2. Methane (c_1), ethylene (c_2), acetylene (c_3), benzene (c_4) and hydrogen (c_5) were considered in the reaction model.

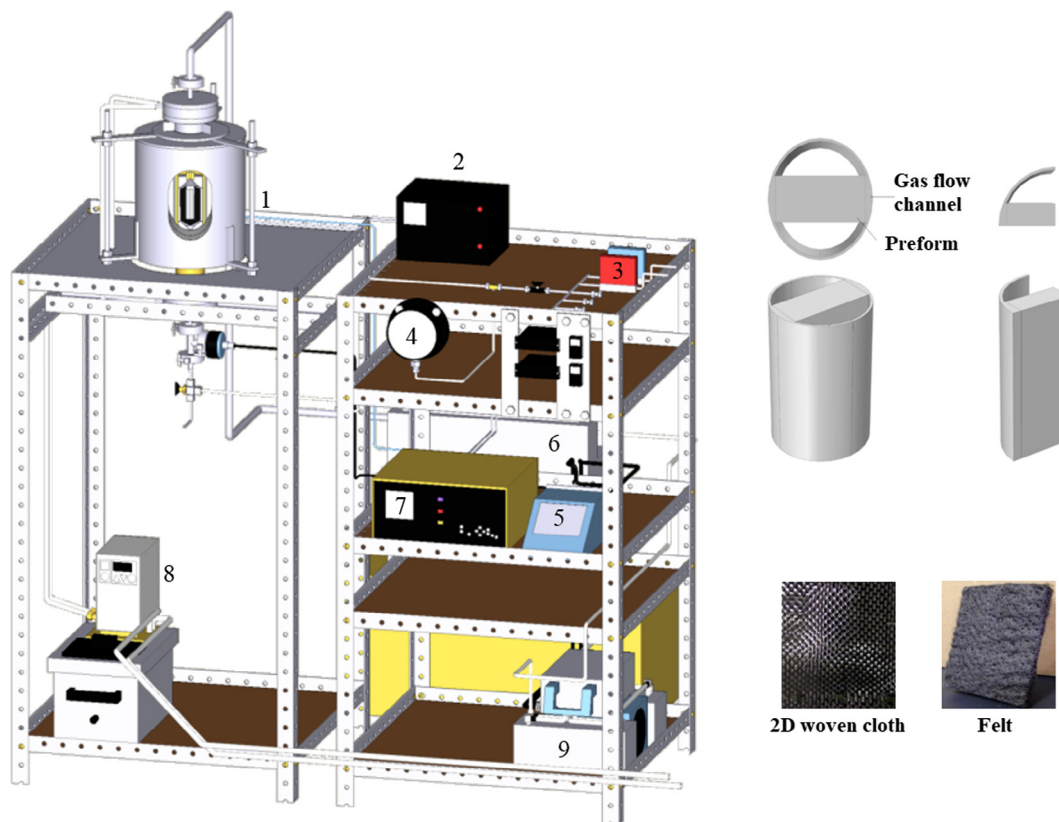


Fig. 1. Schematic diagram of the laboratory-scale CVI reactor and simplified 3D axial symmetry geometry for the laboratory scale CVI reactor. 1. Furnace; 2. High temperature warning device; 3. Mass flow controller; 4. Pressure gauge with contact; 5. Pressure controller; 6. Cold trap; 7. Temperature controller; 8. Cooling water circulator; 9. Vacuum pump.

Methane was consecutively converted into soot in the gas phase, and pyrocarbon was deposited from ethylene, acetylene, and benzene. Meanwhile, hydrogen inhibition coefficients I_{c_2} , I_{c_3} , and I_{c_4} were applied to modify the kinetic data of the surface reactions. k_i denotes the reaction rate constant for the reaction i . The reaction kinetic data in Arrhenius format and the hydrogen inhibition coefficients were derived from our previous work (Li et al., 2005; Li and Deutschmann, 2007).

3.2. Pore structure evolution

2D woven cloth and randomly distributed felt were infiltrated in the experiments. The porous preforms are progressively densified during the CVI process, which leads to the variation of the structural characteristics of the preform. Accordingly, it influences the gas phase diffusion and pyrocarbon deposition inside the pre-

form. Therefore, structural parameters, such as surface area to volume ratio (S_v), pore size (r_p), tortuosity (τ) and porosity (ξ), were introduced into the pore structure evolution model. The computational tool Geodict (Math2Market, Kaiserslautern, Germany) was used to visualize the pore structure evolution of the preforms during the CVI process, and the related structural parameters were given by the tool numerically.

To reproduce the porous structure of the preform in three dimensions, we approximated the carbon preform as a porous body and provided a digital representation of the preform as a set of voxels. The 2D woven cloth with a volume of $700 \times 700 \times 414$ voxels was generated to replace the structure of the cloth preform in three dimensions, while the randomly distributed felt with a volume of $256 \times 256 \times 256$ voxels was generated, as shown in the second column of Table 1. In this study, the computational grid consists of cubic grid cells, and thus a voxel length of $1 \mu\text{m}$ is required.

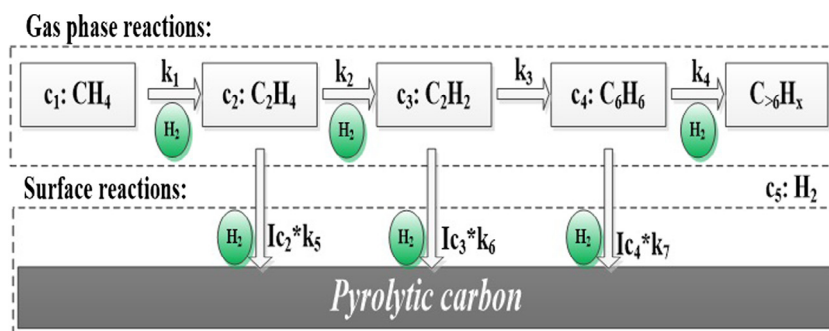


Fig. 2. Multi-step chemical reaction model considering the hydrogen inhibition.

Assuming the deposited pyrocarbon grows uniformly and virtually on the carbon fibre surface, i.e., the approximation of the growing deposited pyrocarbon, the densification process was well visualized with the deposited carbon (in green color) surrounding the carbon fibre (in red color) during the progress of CVI, as shown in Table 1. In the case of cloth preform, the deposited pyrocarbon thickness gradually increases from 0 μm to 63 μm , corresponding to the decrease of the porosity from 64.37% to 7.86%. In the case of felt preform, the deposited pyrocarbon thickness gradually increases from 0 μm to 45.5 μm , corresponding to the decrease of the porosity from 93.0% to 0.02%.

Fig. 3 predicts the variation tendency of S_v as a function of ξ for the cloth and felt preforms, and the overlap between fibres during the densification process was considered in the pore structure evolution model. As for the 2D woven cloth, the non-random preform architecture results in a two-pore size distribution, namely, micro-channels within a bundle of fibres and macro-chambers between bundles. The S_v value slumps sharply first, which is due to the filling of the micro-channels within bundles. When the value of the porosity reduces to less than 44%, the S_v value declines slightly due to the filling of the macro-chambers between bundles. For the felt preform with randomly distributed and non-overlapping fibres, S_v climbs steadily to a maximum value and then falls gradually during the pyrocarbon densification. According to Fig. 3, the dependence of S_v on porosity is significantly influenced by the preform structure. We approximated the dependence of S_v as a function of porosity using polynomial fitting, which was subsequently used in the CVI simulation.

Fig. 4 gives the pore distribution profiles of preforms with variable porosities. The pore distribution profile varies widely for different preforms. For the cloth preform, two peaks exist in the pore distribution profile before the infiltration, corresponding to the volume fractions of the macro-chambers between bundles and the micro-channels within a bundle. When $\xi = 0.37$, the small peak representing the micro-channels disappears, and the peak for the macro-chambers moves left. Thereafter, the infiltration process of the pyrocarbon mainly occurs in the macro-chambers. For the felt preform, there exists various pore sizes from 1 μm to 100 μm , and the pore size range gradually narrows down during the infiltration process. According to Fig. 4, the relationship between the equivalent diameter of pore and porosity was obtained, which was the useful input data for our simulation.

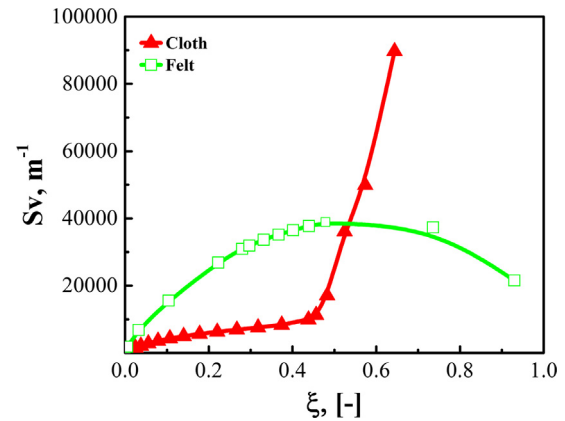


Fig. 3. Evolution of S_v of preforms as functions of porosity.

Tortuosity is an important geometrical parameter as it is used to compute the effective diffusion coefficient of the gaseous species inside the porous preform (Epstein, 1989). The DiffuDict module of GeoDict was applied to calculate the bulk tortuosity of the preform, as plotted in Fig. 5. For the cloth preform, the tortuosity was analysed only at the early stage of pyrocarbon deposition inside the micro-channels, i.e., the porosity of preform is higher than 44%. That is because Knudsen diffusion can be eliminated due to the large enough diameter of the macro-chambers (100.0–1000.0 μm) compared to the mean free path of the molecules when the pyrocarbon is infiltrated in the macro-chambers. Therefore, the tortuosity of the preform is not needed to obtain the effective diffusivity of the gaseous species. The molecular diffusivities of the gaseous species in the macro-chambers are treated as the diffusivities inside the cloth preform when the porosity is less than 44%. For the felt preform, the tortuosity increases during the infiltration process, especially when the porosity is less than 20.0%.

3.3. Mass transfer

Convection and diffusion are considered for the mass transfer of the gaseous species in the gas flow channel of the CVI reactor. The gas flow in the channel outside the preform is assumed to be laminar flow due to the low Reynolds number. Coupling the Navier-

Table 1
Variation of preform structure by CVI using a computational tool for visualizing fibre structures.

Pyrocarbon thickness, μm (Porosity, %)	0(64.37)	14(37.43)	28(26.69)	63(7.86)
Cross section of one fibre				
Cloth preform				
Pyrocarbon thickness, μm (Porosity, %)	0(93.00)	13(47.90)	26(10.40)	45.5(0.02)
Cross section of one fibre				
Felt preform				

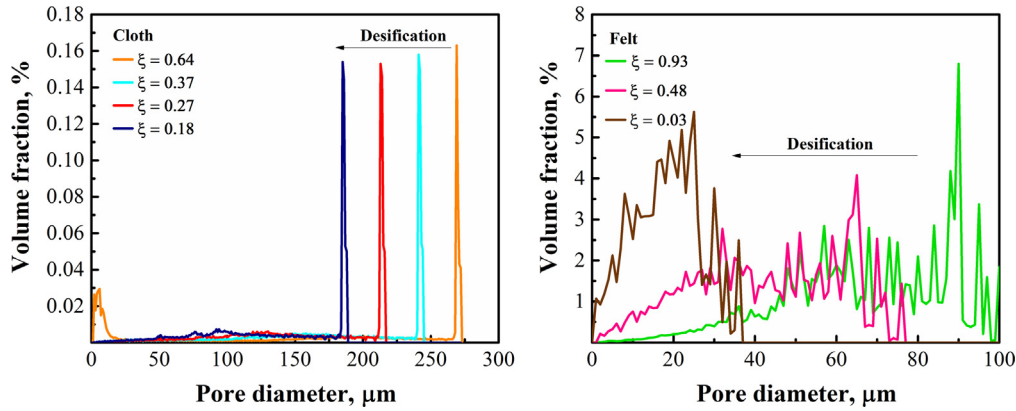


Fig. 4. Pore distribution profiles of the preforms with variable porosities.

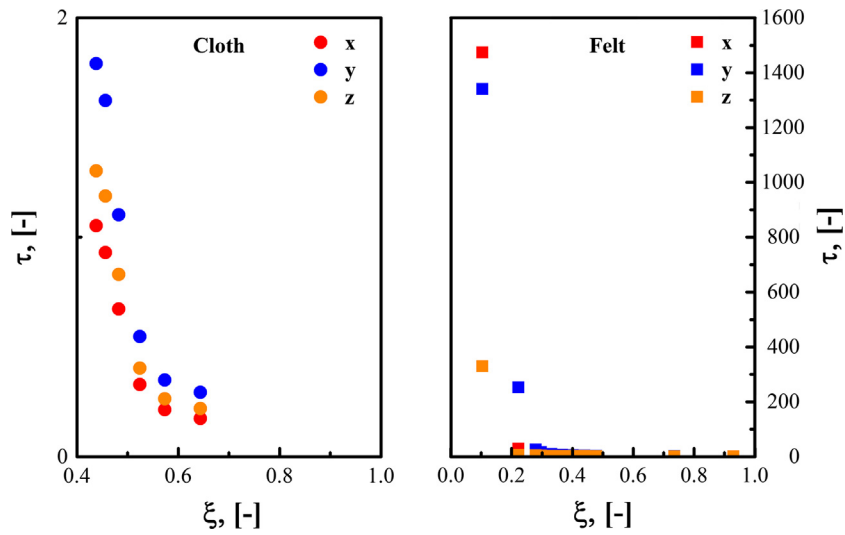


Fig. 5. Bulk tortuosities of the preforms with variable porosities.

Stokes equation of the laminar flow with the convection–diffusion equations, the mass transfer of the gaseous species in the narrow channel was analysed. The Chapman–Enskog equation is used to estimate viscosity for a dilute gas. The transport collision integral $\Omega(T^*)$ for the Lennard–Jones (12–6) potential as a function of the reduced temperature T^* is derived from Neufeld et al. (1972).

$$\mu = 2.6693 \times 10^{-6} \frac{(M_1 T)^{1/2}}{\delta^2 \Omega(T^*)}$$

$$T^* = \kappa T / \varepsilon$$

As for the mass transfer of the gaseous species inside the preform, molecular diffusion and Knudsen diffusion are included. Molecular diffusivity is given by the empirical equation of Fuller–Gidding, which considers interactions between methane and each chemical species in the gas phase. Knudsen diffusion is introduced when the pore size inside the preform is comparable to the mean free path of the gas-phase molecules. Consequently, the effective diffusivity equation gives:

$$D_i = 10^{-7} \frac{T^{1.75} \sqrt{\frac{M_i + M_5}{M_i M_5}}}{p \left[\sum V_i^3 + \sum V_5^3 \right]^{1/2}}$$

$$D_i^k = 97 * r_p * \sqrt{\frac{T}{M}}$$

$$D_i^{eff} = \frac{D_i * D_i^k}{D_i + D_i^k}$$

Combing the structural parameters obtained in Part 3.2 with the equations given above, the effective diffusivities of the selected gas-phase species inside the preforms as functions of porosity are calculated in three dimensions, as shown in Fig. 6. The effective diffusivities of the gaseous species inside the cloth preforms are considered only when the micro-channels are infiltrated at the early stage of CVI process. However, the effective diffusivities of the gaseous species inside the felt preform are computed throughout the infiltration process.

3.4. Governing equations

Transient 3D simulation of the CVI process includes subdomains of the gas flow channel Ω_1 and the preform Ω_2 . For the gas flow channel, the incompressible Navier–Stokes equation and convection–diffusion equation are applied to describe the velocity field and the concentration field in the channel, respectively. For the preform, the equations describe the gaseous species concentrations, the average density and porosity of the deposited preforms during the CVI process. The governing equations for the CVI simulation are shown below:

Gas flow channel Ω_1 :

$$\begin{cases} \rho(\mathbf{u} \cdot \nabla) \mathbf{u} = \nabla \cdot [-p\mathbf{I} + \mu(\nabla \mathbf{u} + (\nabla \mathbf{u})^T)] \\ \frac{\partial c_i}{\partial t} + \nabla \cdot (-D_i \nabla c_i) + \mathbf{u} \cdot \nabla c_i = R_i, \quad i = 1, 2, 3, 4, 5 \end{cases} \quad (3)$$

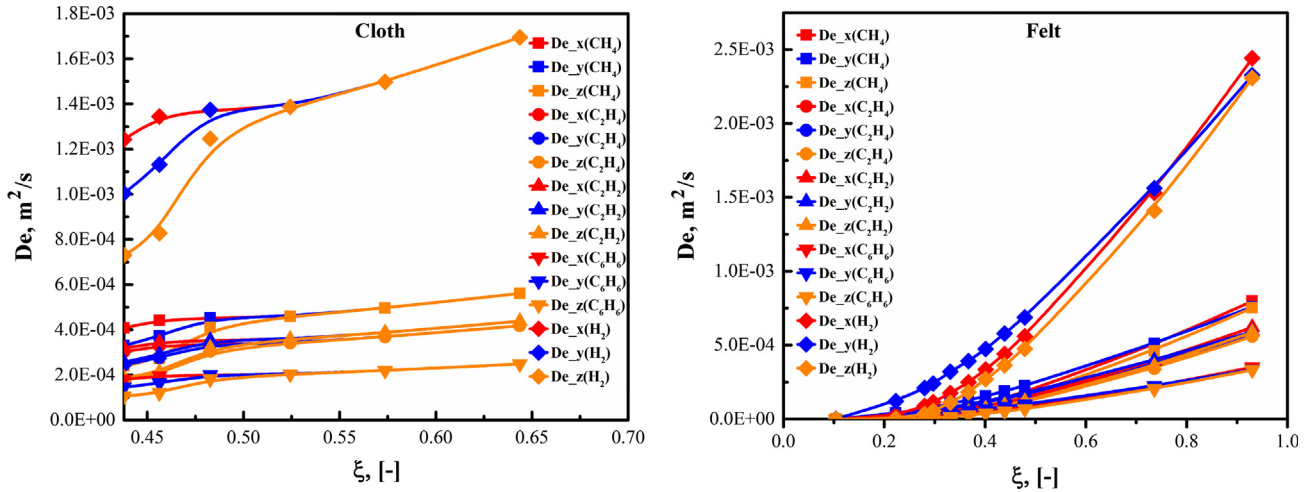


Fig. 6. Bulk effective diffusivities of gaseous species within the preforms with variable porosities.

Preform Ω_2 :

$$\begin{cases} \frac{\partial c_i}{\partial t} + \nabla \cdot (-D_i^{eff} \nabla c_i) = R_i'_{(sv)}, & i = 1, 2, 3, 4, 5 \\ \frac{\partial \rho}{\partial t} = M_C \cdot R_{C(sv)} \\ \frac{\partial \xi}{\partial t} = -\frac{M_C}{\rho_C} R_{C(sv)} \end{cases} \quad (4)$$

where R_i and $R_i'_{(sv)}$ ($\text{mol m}^{-3} \text{s}^{-1}$) represent the chemical reaction term of the gas phase species i in the channel and the preform, respectively. $R_{C(sv)}$ denotes the reaction rate of pyrocarbon deposition. More details about the equation system and the related reaction model of the CVI process can be found in our previous work (Li et al., 2005, 2008; Li and Deutschmann, 2007). Then the equation system can be solved using the following boundary and initial conditions:

$$\begin{cases} u = u_0 \text{ at } \partial\Omega_1^{inlet} \\ c_i = c_0 \text{ and } c_i = 0 \text{ for } i = 2, \dots, 5 \text{ at } \partial\Omega_1^{inlet} \\ -n \cdot D_i \nabla c_i = 0 \text{ for } i = 2, \dots, 5 \text{ at } \partial\Omega_1^{outlet} \\ \rho|_t = 0 = \rho_0 \text{ in } \partial\Omega_2 \\ \xi|_t = 0 = \xi_0 \text{ in } \partial\Omega_2 \end{cases} \quad (5)$$

4. Results and discussion

Fig. 7 illustrates the predicted results of the density distribution of the cloth and felt preforms with increasing deposition time from 12-h to 120-h. For the cloth preform, the density is increased from the outside to the inside, which indicates that the preform is well infiltrated during the CVI process. However, for the felt preform, there exist higher density regions at the bottom right corner and the upper part of it after a 48-h deposition time. These regions have a certain obstructive effect on the gaseous species to transport into deep parts of the preform, increasing the tendency of the formation of surface sealing. Especially, after a 120-h deposition, the surface sealing apparently appears at the surface of the upper part of the felt preform. For both preforms, a low-density region appears at the bottom left corner, corresponding to the low deposition rate in this area, which is due to the excess of the immature gas-phase precursors for the pyrocarbon deposition near the inlet of the narrow channel. The final bulk density for the cloth preform is 1.629 g/cm^3 and 1.656 g/cm^3 for the felt preform after a 120-h deposition time, according to the computation result.

The average bulk densities of the infiltrated samples were measured by the draining method at room temperature. Fig. 8 shows

the comparison between the experimental and simulated results of the bulk density for the preforms as a function of the deposition time. Obviously, the deposition rate of the felt preform is much higher than that of the cloth preform at the initial deposition stage. The predicted results agree well with the experimental results for the felt preform. However, the experimental results of the density distribution illustrate that the pyrocarbon was homogeneously infiltrated inside the felt preform, which shows a slight discrepancy with the predicted results. For the cloth preform, there are some numerical disparities compared to the experimental results. These disparities may be attributed to the simplified reaction model used here, which is not able to accurately predict the gas-phase compositions. Overall, the variation tendency of the bulk density for both preforms can be well revealed by the present simulated results. In Fig. 9, the comparison between the experimental and the predicted results of the porosity variation for the preforms as a function of deposition time is also displayed. For both preforms, the predicted results agree well with experimental results and the porosity decreases with the deposition time. After a 29-h infiltration time, the micro-channels inside the cloth preform are almost filled by the deposited pyrocarbon, according to the computation. According to the experimental results, the final porosities for the cloth and felt preforms after a 120-h infiltration time are 0.150 and 0.240, respectively. It is very likely that the simulation can reproduce the results of the experiments, and the different trends observed for different preform structures during the densification process are captured successfully.

Lieberman and Pierson (Lieberman and Pierson, 1974; Pierson and Lieberman, 1975) suggested that the concentration ratio $R = [C_2H_x]/[C_6H_y]$ in the gas phase significantly affects the pyrocarbon texture. The guideline approximately follows that $R < 5$ corresponds to the medium textured pyrocarbon, $5 < R < 70$ to the high textured pyrocarbon, and $R > 70$ to the isotropic pyrocarbon. Here, $R^* = [C_6H_6]/[C_2H_x]$ is used, which denotes the maturity of the gas-phase species. Meanwhile, the deposition rate of C_6H_6 is higher than that of C_2H_x (C_2H_4 , C_2H_2). Therefore, the R^* ratio can be related to the bulk density distribution of the C/C composite. Fig. 10 illustrates the simulated results of the R^* ratio distribution in the free flow channel and the preforms after a 1-h and 96-h deposition. The R^* ratio distribution for the 96-h deposition time is relatively higher than that in the initial deposition time. In addition, the region with a high R^* ratio represents the highly densified part of the preform, which is coherent with the simulated results of the density distribution in the preforms. According to the predicted profiles of R^* in Fig. 10, the values of R for both preforms are all less

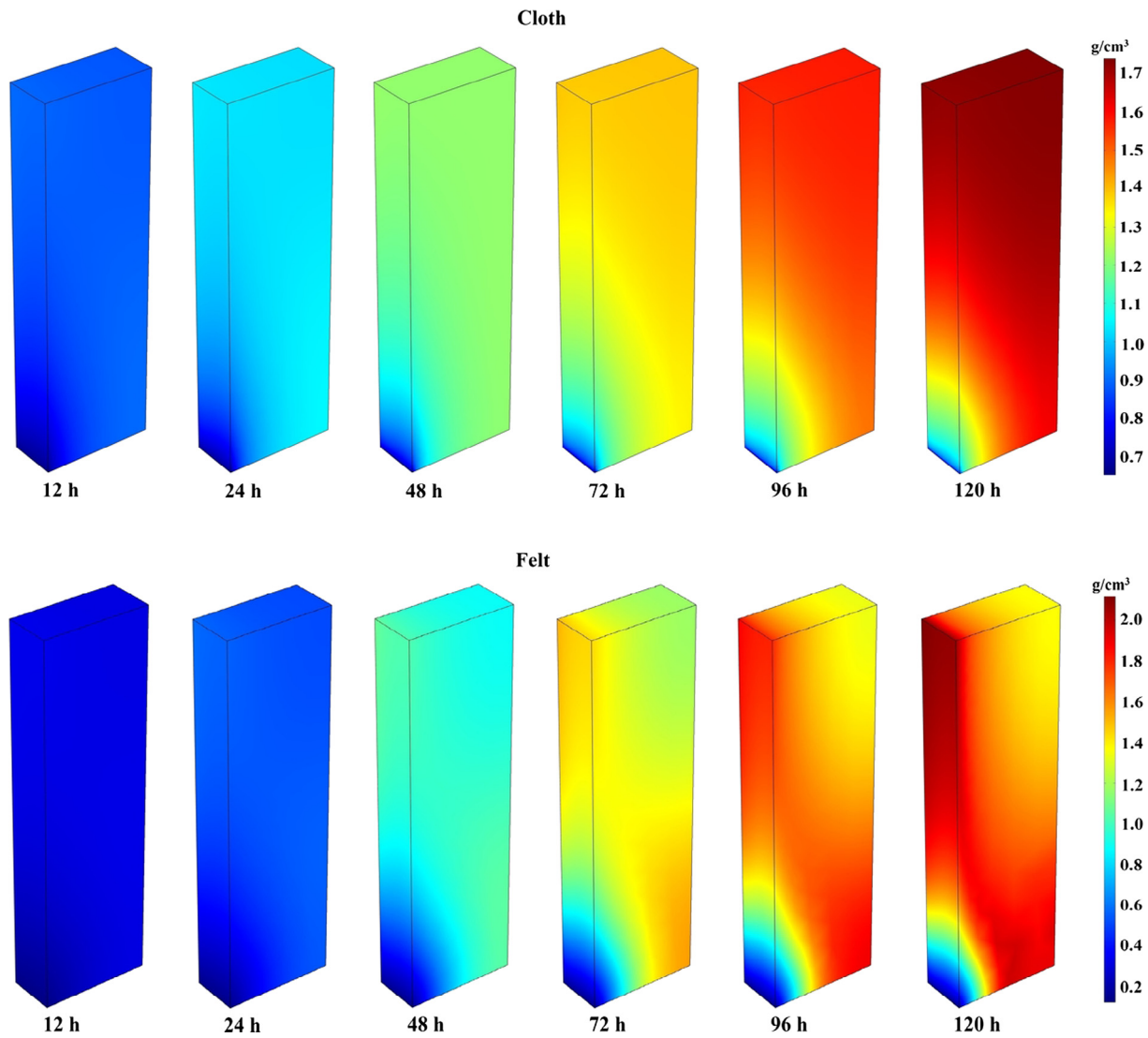


Fig. 7. Predicted bulk density distributions as a function of deposition time in the CVI reactor using woven cloth and felt as preforms (left side of the preforms is close to the gas flow channel).

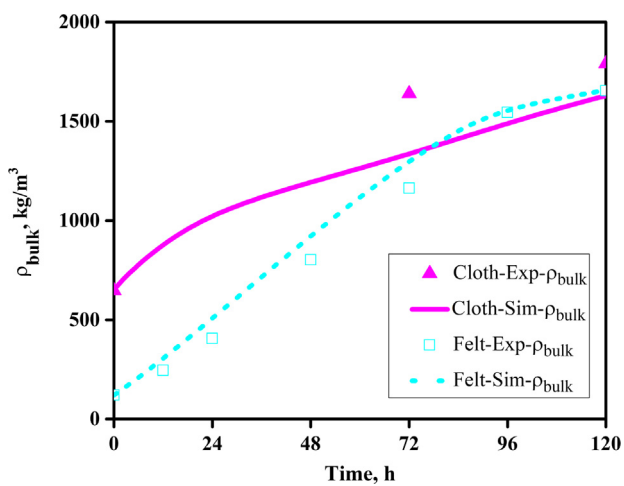


Fig. 8. Comparison of the measured material density with the predicted value obtained using the simulation as a function of deposition time.

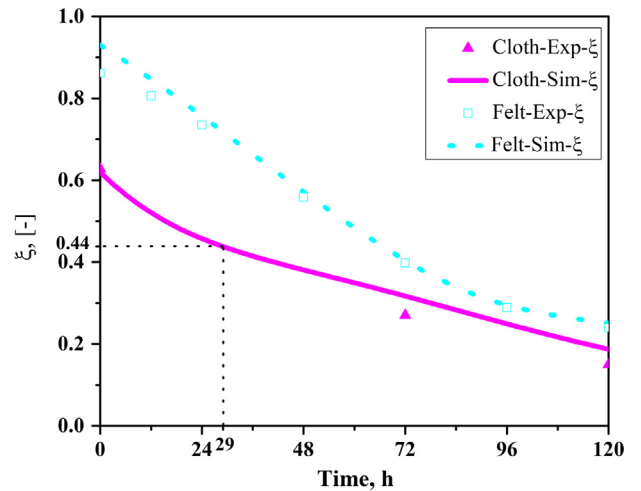


Fig. 9. Comparison between experimental and predicted porosities for the cloth and felt preforms as a function of deposition time.

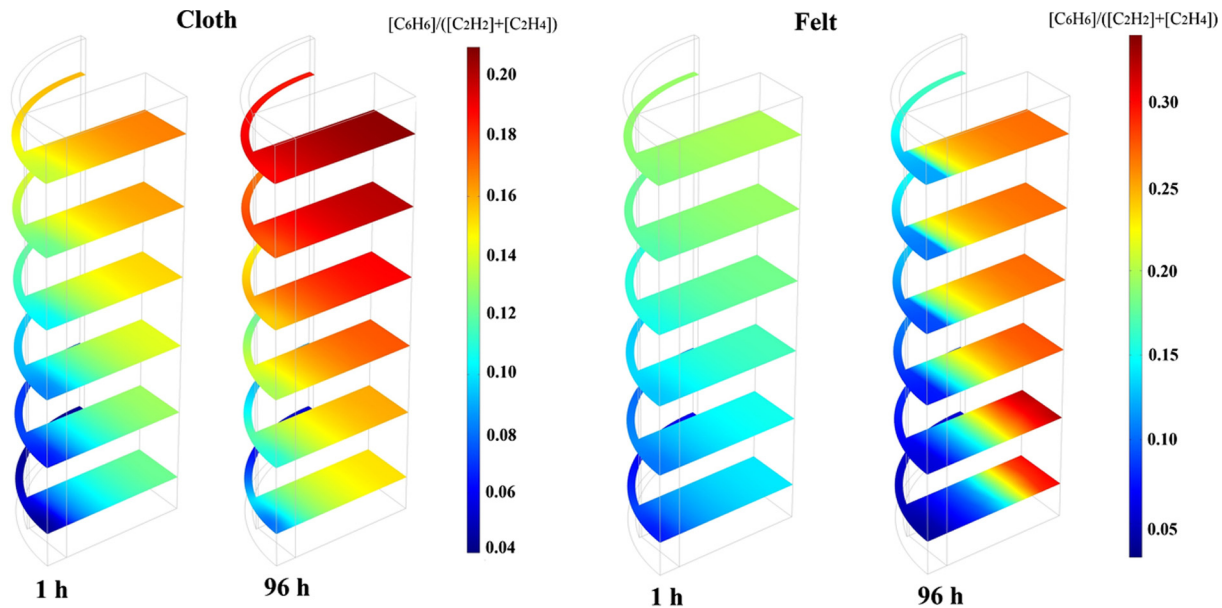


Fig. 10. Simulated results of the concentration ratio of benzene to acetylene and ethene for preforms after a 1-h and 96-h deposition time.

than 25 for 1-h and 96-h infiltration time. Therefore, we predict that the medium textured and high textured pyrocarbon were deposited inside both preforms.

5. Conclusions

Preforms of 2D woven cloth and randomly distributed felt were infiltrated in the given experimental conditions. A software tool was applied to reproduce the 3D digital structure of the two preforms. The pore structure evolution model and related 3D structural characteristics of the preforms were obtained by approximating the growing solid phase during the CVI process. Combining the detailed structural characteristics with the multi-step chemical reaction model, the transient 3D simulation of the CVI process for the two preforms was successfully implemented. The predicted results of the bulk density of preforms agree well with the experimental results. However, the deviation between the experimental and simulated results of the cloth preform is relatively high. Therefore, except for the detailed mass transport modelling that we have proposed here, the detailed reaction mechanism, including the gaseous species and surface species with an acceptable scale, is needed to rebuild the previous models.

Acknowledgements

Financial support from the program of China Scholarships Council is gratefully acknowledged.

References

Becker, A., Hüttinger, K.J., 1998. Chemistry and kinetics of chemical vapor deposition of pyrolytic carbon-III pyrolytic carbon deposition from propylene and benzene in the low temperature regime. *Carbon* 36, 201–211.

Besmann, T.M., Sheldon, B.W., Lowden, R.A., Stinton, D.P., 1991. Vapor-phase fabrication and properties of continuous-filament ceramic composites. *Science* 253, 1104–1109.

Besmann, T.M., Matlin, W.M., Stinto, D.P., 1996. Chemical vapor infiltration process modeling and optimization. In: Hepp, A.F., Kumta, P.N., Sullivan, J.J., Fischman, G.S., Kaloyeros, A.E. (Eds.), *Covalent Ceramics III – Science and Technology of Non-Oxides*, MRS Symposium Proceedings, Materials Research Society, vol. 410. Pittsburgh, PA, pp. 441–451.

Birakayala, N., Evans, E.A., 2002. A reduced reaction model for carbon CVD/CVI process. *Carbon* 40, 675–683.

Chand, S., 2000. Review carbon fibers for composites. *J. Mater. Sci.* 35, 460–463.

Coindreau, O., Mulat, C., Germain, C., Lachaud, J., Vignoles, G.L., 2011. Benefits of X-ray CMT for the modeling of C/C composites. *Adv. Eng. Mater.* 13, 178–185.

Currier, R.P., 1991. Overlap model for chemical vapor infiltration of carbon in porous carbon substrate. *Carbon* 29, 387–396.

Delhaes, P., 2002. Chemical vapor deposition and infiltration processes of carbon materials. *Carbon* 40, 641–657.

Epstein, N., 1989. On tortuosity and the tortuosity factor in flow and diffusion through porous media. *Chem. Eng. Sci.* 44, 777–779.

Fitzer, E., 1987. The future of carbon-carbon composites. *Carbon* 25 (2), 163–190.

Golecki, I., 1997. Rapid vapor-phase densification of refractory composites. *Mat. Sci. Eng. R.* 20, 37–124.

Guan, K., Cheng, L., Zeng, Q., Zhang, L., Deng, J., Li, K., Li, H., 2013. Modeling of pore structure evolution between bundles of plain woven fabrics during chemical vapor infiltration process: the influence of preform geometry. *J. Am. Ceram. Soc.* 96, 51–61.

Ibrahim, J., Paolucci, S., 2011. Transient solution of chemical vapor infiltration/deposition in a reactor. *Carbon* 49, 915–930.

Kastner, J., Plank, B., Reh, A., Salaberger, D., Heinzl, C., 2012. Advanced X-Ray tomographic methods for quantitative characterization of carbon fibre reinforced polymers. In: *4th International Symposium on NDT in Aerospace*. Augsburg, pp. 1–9.

Kinney, J.H., Breunig, T.M., Starr, T.L., Haupt, D., Nichols, M.C., Stock, S.R., Butts, M.D., Saroyan, R.A., 1993. X-ray tomographic study of chemical vapor infiltration processing of ceramic composites. *Science* 260, 789–791.

Li, A., Deutschmann, O., 2007. Transient modeling of chemical vapor infiltration of methane using multi-step reaction and deposition models. *Chem. Eng. Sci.* 62, 4976–4982.

Li, A., Norinaga, K., Zhang, W., Deutschmann, O., 2008. Modeling and simulation of materials synthesis: chemical vapor deposition and infiltration of pyrolytic carbon. *Compos. Sci. Tech.* 68, 1097–1104.

Li, H., Li, A., Bai, R., Li, K., 2005. Numerical simulation of chemical vapor infiltration of propylene into C/C composites with reduced multi-step kinetic models. *Carbon* 43, 2937–2950.

Lieberman, M.L., Pierson, H.O., 1974. Effect of gas phase conditions on resultant matrix pyrolytic carbons in carbon/carbon composites. *Carbon* 12, 233–241.

Neufeld, P.D., Janzen, A.R., Aziz, R.A., 1972. Empirical equations to calculate 16 of the transport collision integrals $(l, s)^*$ for the Lennard-Jones (6–12) potential. *J. Chem. Phys.* 57, 1100–1102.

Norinaga, K., Deutschmann, O., 2007. Detailed kinetic modeling of gas-phase reactions in the chemical vapor deposition of carbon from light hydrocarbons. *Ind. Eng. Chem. Res.* 46, 3547–3557.

Panerai, F., Ferguson, J., Lachaud, J., Martin, A., Gasch, M.J., Mansour, N.N., 2015. Analysis of fibrous felts for flexible ablators using synchrotron hard X-ray microtomography. In: *8th European Symposium on Aerothermodynamics for Space Vehicles*, Paper No. 89747, Lisbon, Portugal, 2015, pp. 1–8.

Pfrang, A., Schladitz, K., Wiegmann, A., Schimmel, T., 2007. Calculation of the evolution of surface area and free volume during the infiltration of fiber felts. *Chem. Vapor. Depos.* 13, 705–715.

- Pierson, H.O., Lieberman, M.L., 1975. The chemical vapor deposition of carbon on carbon fibers. *Carbon* 13, 159–166.
- Roman, Y.G., Stinton, D.P., 1995. Ceramic matrix composites – advanced high-temperature structural materials. In: Lowden, R.A., Ferber, M.K., Hellmann, J.R., Chawla, K.K., Dipietro, S.G. (Eds.), *MRS Symposium Proceedings Series*. Materials Research Society, Boston, pp. 343–350.
- Starr, T.L., 1995. Gas transport model for chemical vapor infiltration. *J. Mater. Res.* 10, 2360–2366.
- Tang, Z., Li, A., Zhang, Z., Ma, X., Wang, W., Fang, J., Bai, R., 2014. Chemistry and kinetics of heterogeneous reaction mechanism for chemical vapor infiltration of pyrolytic carbon from propane. *Ind. Eng. Chem. Res.* 53, 17537–17546.
- Vignoles, G.L., Baconneau, O., Brauner, C.M., 2001. Interaction between gas diffusion and multistable heterogeneous chemical kinetics in C/C composite processing. In: *Fundamentals of Gas-Phase and Surface Chemistry of Vapor-Phase Deposition II/Process Control, Diagnostics and Modeling in Semiconductor Manufacturing IV*, in ECS Proceedings, Washington, Pennington, NJ, USA: The Electrochemical Society, 13, 237–244.
- Vignoles, G.L., Ducloux, R., Gaillard, S., 2007. Analytical stability study of the densification front in carbon- or ceramic-matrix composites processing by TG-CVI. *Chem. Eng. Sci.* 62, 6081–6089.
- Vignoles, G.L., 2015a. Chemical vapor deposition/infiltration processes for ceramic composites. In: Boisse, P. (Ed.), *Advances in Composites Manufacturing and Process Design*. Woodhead Publishing, France, pp. 147–176.
- Vignoles, G.L., 2015b. Modeling of chemical vapor infiltration processes. In: Boisse, P. (Ed.), *Advances in Composites Manufacturing and Process Design*. Woodhead Publishing, France, pp. 415–458.
- Wu, S., Yi, M., Ge, Y., Ran, L., Peng, K., 2017. Effect of carbon fiber reinforcement on the tribological performance and behavior of aircraft carbon brake discs. *Carbon* 117, 279–292.
- Yan, X., Xu, Y., 2010. *Chemical Vapour Deposition: An Integrated Engineering Design for Advanced Materials*. Springer, UK, London, pp. 165–213.
- Zhang, W., Hüttinger, K.J., 2001. Chemical vapor infiltration of carbon-revised, Part I: Model simulations. *Carbon* 39, 1013–1022.